Received: 30 September 2018 | Revised: 29 April 2019 | Accepted: 1 August 2019

DOI: 10.1002/we.2409

RESEARCH ARTICLE

WILEY

Spectral analysis of New MEXICO standstill measurements to investigate vortex shedding in deep stall

Muhammad A. Khan[1,3] | Carlos Simão Ferreira[1] | Gerard J. Schepers[2] | Niels N. Sørensen[3]

[1] Aerospace Department, Delft University of Technology, Delft, The Netherlands

[2] Unit Wind Energy, Energy research Centre of the Netherlands (ECN part of TNO), Petten, The Netherlands

[3] Wind Energy Department, Technical University of Denmark, Lyngby, Denmark

Correspondence
Muhammad A. Khan, Aerospace Department, Delft University of Technology, Kluyverweg 1, 2629 HS Delft, The Netherlands.
Email: arsalankhanji@gmail.com

Carlos Simão Ferreira, Wind Energy Section, Kluyverweg 1, 2629 HS Delft, The Netherlands.
Email: c.j.simaoferreira@tudelft.nl

Funding information
Energy Research Center of the Netherlands

Abstract

Spectral analysis was performed on the time series data computed from pressure measurements on the New MEXICO (Model Rotor Experiments under Controlled Conditions) rotor in standstill conditions. As a priori, 3D airfoil polars were recreated from standstill measurements and compared against 2D airfoil polars and flat plate theory results to verify the measurements. The spectral analysis revealed the presence of dominant shedding frequencies for certain ranges of the geometric angle of attack. Two dominant shedding modes were identified: One was associated with bluff body vortex shedding, and the other was associated with low Strouhal number shedding. No dominant shedding frequencies were observed for angles of attack beyond 50°. The research improves on our current understanding of the unsteady nature of the stall regime, along with providing insight into the existence of vortex-induced vibrations on a wind turbine in standstill conditions.

KEYWORDS

3D airfoil polars, aerodynamics, stall, vortex shedding, wind turbines

1 | INTRODUCTION

In modern times, sustainable energy resources like wind power might be the answer to global warming and air pollution. However, they need to contend against conventional fossil fuel–based energy systems on an economical front. Therefore, the levelized cost of wind energy needs to continue to decrease, and the social acceptance towards wind energy needs to increase. Realizing this goal solicits a trend in developing larger wind turbines. Development of larger wind turbines requires improved aeroelastic tools that can accurately predict the complex aerodynamics, elastic deformations, and inertial dynamics, which is representative for these behemoth structures. Wind turbines frequently operate at off-design conditions during their life cycle and undergo dynamic loads characterized by unsteady aerodynamics. Predicting these unsteady aerodynamic loads has been very difficult because of the nonlinear nature of unsteady aerodynamics. Especially when operating near the stall region and in deep stall, these turbines are prone to increased loads because of the dynamic nature of stall.

Generally, above the cut-off wind speed, a wind turbine will initiate a shut down phase. During this phase, the rotor blades are pitched into the wind and parked; hence, the wind turbine is in standstill mode. In standstill, a wind turbine might not have yaw control. Therefore, a change in wind direction can result in extremely large angle of attack (AoA), blade loads, and possibly stall- or vortex-induced vibrations. Stall-induced vibrations occur at large AoA beyond static stall, where the lift curve slope is negative. Typically, this results in negative aerodynamic damping for the edgewise mode of vibration.[1] On the

NOMENCLATURE: α, angle of attack; α_{geo}, geometric angle of attack; α_{geo}, yaw angle for a wind turbine rotor; θ, pitch angle for a wind turbine rotor; Ω, rotor rotational speed; c, chord length; C_d, drag coefficient; C_l, lift coefficient; F_n, normal force on a blade section; F_t, tangential force on a blade section; f, frequency; L_{char}, characteristic length; p, gauge pressure from pressure ports; St, Strouhal number; t, airfoil thickness; U_∞, free-stream velocity; V, in-plane local inflow velocity for a blade section.

contrary, vortex-induced vibrations are expected to happen close to 90° AoA because of the shedding of von Karman vortex street. When this periodic shedding of vortices matches the natural frequency of the blade, a lock-in phenomenon[2] can result, whereby the blade structural motion controls the vortex shedding frequency within a certain threshold of inflow conditions. Vortex-induced vibration is still a topic under debate as it has not been well-documented on wind turbines, although researchers have found possible evidence of its occurrence through numerical simulations. Zou et al[3] performed numerical simulations on a 2D elastically mounted airfoil section using a vortex type model. Their vortex model was based on the "double wake" concept to accurately model the physics of separated flow. They observed large vortex-induced vibrations when the first edgewise natural frequency coincides with the vortex shedding frequency. Skrzypiǹski et al[4] performed 2D and 3D computational fluid dynamics (CFD) computations on a DU96-W-180 airfoil at 90° AoA to analyze vortex-induced vibrations. They used non-moving, prescribed motion, and elastically mounted airfoil section for computations. Negative aerodynamic damping close to stationery vortex shedding frequencies was found along with high probability of lock-in phenomenon for airfoils. However, both these studies neglected the 3D geometry of a modern wind turbine blade and employed simplification to the structural model as well. More recently, Heinz et al[2] conducted an in-depth analysis on the existence of vortex-induced vibrations for modern wind turbines. The DTU 10 MW reference wind turbine was used to perform high fidelity aeroelastic simulations in the deep stall regime using HAWC2CFD.[5] HAWC2CFD is an aeroelastic coupling between multibody structural solver of HAWC2[6] with the CFD solver EllipSys3D.[7,8] Computations were performed using detached eddy simulation. Using realistic inflow conditions, they were able to identify severe edgewise blade vibrations due to vortex shedding phenomenon. Therefore, the importance of vortex-induced vibrations cannot be neglected for large wind turbines of the future. Currently, there have not been many efforts in developing an engineering model that tries to model unsteady loads originating from vortex shedding phenomenon. Previously, Snel[9] had hypothesized existence of self-excited dynamic stall due to vortex shedding and had tried to include it in his dynamic stall model. Another effort was made by Bertagnolio et al,[10,11] where they used a stochastic model to represent vortex shedding and airfoil wake turbulence. The model uses experimental or CFD measurements as input data. However, the model was not able to accurately predict vortex shedding frequencies.

The purpose of the current research was to investigate vortex shedding of self-excited nature using measurements, because it is important to gather experimental evidence to support the ongoing research on vortex-induced vibrations in standstill conditions. Therefore, in order to shed light on the aerodynamics of a blade in standstill conditions, the new model rotor experiments under controlled conditions (New MEXICO) measurements are a valuable resource. The New MEXICO measurements in standstill were performed for axially aligned flow with and without zigzag tape on the outboard part of the blade ($\frac{r}{R} > 0.7$). The New MEXICO experimental data is particularly attractive for understanding critical flow mechanisms or validating engineering models because it offers a controlled environment with the least possible turbulence levels between 0.2% to 0.4%.[12] Although the New MEXICO measurements have been the subject of extensive research in the past, particularly through IEA Wind Task 29: Mexnext,[13-15] there is still a lack of research on the frequency domain analysis of these measurements. Such an analysis might be able to answer some of the questions regarding the existence of vortex-induced vibrations in a real-world scenario. This is where the current research tries to fill the gap by providing a comprehensive spectral analysis of the New MEXICO standstill measurements.

2 | METHODOLOGY

For the purpose of this research, New MEXICO pressure sensor data was used. The data was recorded in units of pascals and was calibrated for sensor drift by Parra.[16] A preliminary evaluation of data quality was undertaken to access whether there are any large non-physical kinks in blade section pressure profiles. A detailed analysis of the pressure profiles for different test cases can be found in the master thesis report of Khan.[17] Standstill pressure distribution for very large AoA had shown some kinks in pressure distribution. On the contrary, at somewhat lower AoA, but still in the deep stall regime, the measurement quality was reasonable. Hence, it can be said that the quality of standstill measurements deteriorates at large AoA. Therefore, a further analysis of the standstill measurements was performed, whereby 3D airfoil polars were extracted and compared with 2D airfoil polars in Section 3.1.1 to evaluate the relevance of these measurements. A brief description of extracting 3D airfoil polars from standstill measurements is presented in Section 3.1. Moreover, lift to drag ratio computed from 3D polars was also validated with results

TABLE 1 A summary of all the standstill data points in the New MEXICO measurement campaign

Case Type	Data Point	U_∞, m/s	β, degree	θ, degree	Ω, rpm
Axial flow[a]	372-394	~30	0	−2.3-90	0
	397-401				
Yawed flow[a]	405-425	~30	−90, −60, −45, −30, −15	90	0
			+15, +30		
Axial flow[b]	905-925	~30	0	60-90	0

Abbreviation: MEXICO, model rotor experiments under controlled conditions.

[a]With zigzag tape on outboard part of the blade ($\frac{r}{R} > 0.7$).

[b]Without zigzag tape on outboard part of the blade ($\frac{r}{R} > 0.7$).

from flat plate theory in Section 3.1.2. This procedure helped in establishing confidence in the New MEXICO standstill measurements. Previously, in comparison, the old MEXICO standstill measurements had bad data quality, rendering it unusable for a frequency domain analysis.

Once having established confidence in New MEXICO standstill measurements, the research focused on computing normal and tangential forces from pressure sensor data using the trapezoidal rule of integration, as described in Section 2.1.2, thus giving a time series of normal and tangential forces for every standstill data point presented in Table 1. Each New MEXICO data point corresponds to a test run at one particular set of conditions where data was collected for a duration of 5 seconds. The time signals were de-trended before performing fast Fourier transform to remove the power of DC frequency and focus the analysis on unsteady fluctuations. Subsequently, in Section 3.2, dominant flow frequencies (frequencies with the highest power spectral density) were extracted from each data point at a particular spanwise section and stored against corresponding geometric AoA of that spanwise section. After filtering erroneous frequencies, Strouhal numbers were computed in Section 3.2.2 and plotted against the geometric AoA.

2.1 | Wind tunnel experiments

The original MEXICO experiments were conducted in December 2006 at the large-scale low-speed facility of German-DutchWind Tunnel (DNW). Overall, the experiments were a success, but there were some questions that were left unanswered. Therefore, a proposal for a second MEXICO experiment was forwarded. The New MEXICO experiment was performed in 2014.[18] The New MEXICO experiments used the same three-bladed rotor with a 4.5-m diameter wind tunnel model as with the original MEXICO experiments.[19] The MEXICO rotor is rigid, and it is instrumented with pressure sensors at various locations along the span. In addition, a six-component balance is mounted at the base of the turbine to acquire total forces and moments. The blade cross-section is composed of a "DU 91-W2-250" airfoil near the root, a "RISØ-A1-21" airfoil at the mid span, and a "NACA 64(3)-418" near the tip. In the original MEXICO experiments, a zigzag tape was added at 5% chord both on the suction and pressure side to promote turbulent transition of boundary layer and avoid laminar separation. However, a concern was raised that the zigzag tape might be de-cambering the blade sections by thickening the boundary layer (because of its own thickness),[18] in addition to transitioning to turbulent flow. Therefore, in the New MEXICO experiments, the zigzag tape was removed from the outboard part ($\frac{r}{R} > 0.7$) of the blades for comparison. For further information regarding the New MEXICO model, the report by Boorsma and Schepers[18] can be consulted.

2.1.1 | Instrumentation and data storage

The New MEXICO blades were instrumented with 148 Kulite pressure sensors, which measure the absolute pressure. The sensors were distributed at 25%, 35%, 60%, 82%, and 92% span (spanwise location is defined from the rotor center normalized by the rotor radius, ie, $\frac{r}{R}$) across the three different blades as shown in Table 2. A large number of different measurement were collected at various experimental conditions. For further information regarding the New MEXICO experimental setup and test matrix, the reader is advised to read Boorsma and Schepers.[12]

The pressure data was sampled at a frequency of 5.514 kHz, which gives approximately 27600 sample points for a 5-second measurement run. Spurious sensor data were removed during data reduction, a summary of which is given by Parra.[16] The data was also corrected for sensor drift by taking zero measurements prior to and after a set of runs with a particular measurement configuration. The corrected pressure is also the differential (or gauge) pressure. For further information regarding data reduction and calibration, the reader is referred to Parra,[16] as calibrated data was used for the purpose of the current research work.

2.1.2 | Computing normal and tangential forces

The forces acting on a blade section can be computed through integrating the pressure distributions along the chord using trapezoidal rule of integration. The pressure taps along the blade surface are numbered in a clockwise sense (to preserve consistency with New MEXICO data), as illustrated in Figure 1. Here, the red point at the trailing edge denotes a fictitious pressure tap created at the trailing edge of the blade to prevent discontinuity in the integration process. The value of differential pressure for this fictitious pressure tap is calculated to be the average of the second and N*th* pressure tap.

$$F_{\mathrm{n}} = \sum_{i=1}^{N} \frac{1}{2}(p_i + p_{i+1})(x_i - x_{i+1}), \tag{1}$$

TABLE 2 Location of pressure sensors on the three blades and the relative azimuthal definition for the three blades

Blade No.	Pressure Sensor Location	Relative Azimuth, Degrees[a]	Airfoil Section
1	25% and 35% span	0	DU91-W2-250
2	60% span	−120	RISØ A2-21
3	82% and 92% span	120	NACA-64418

[a]The zero rotor azimuth is defined as the position when blade 1 is at 12 o'clock position.

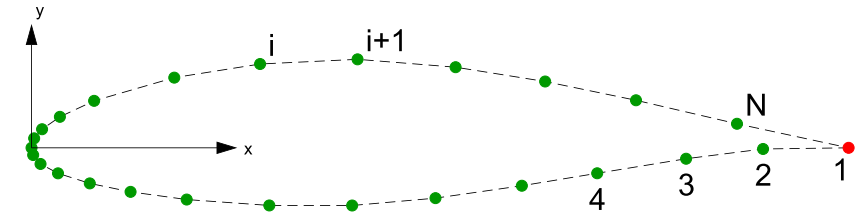

FIGURE 1 The new model rotor experiments under controlled conditions (New MEXICO) blade NACA 64-418 airfoil section with pressure taps highlighted as green points. The red point at the trailing edge is a fictitious pressure tap [Colour figure can be viewed at wileyonlinelibrary.com]

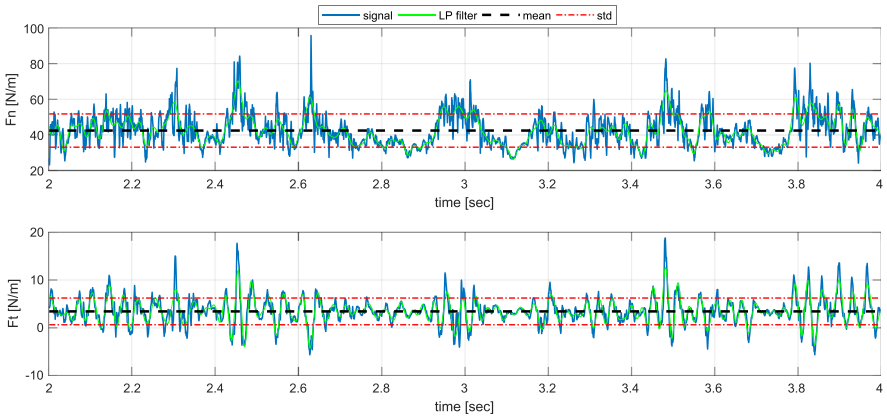

FIGURE 2 Normal force and tangential force variation with time for the 82% spanwise section. A low-pass infinite impulse response (IIR) filter (denoted LP filter) is applied to remove high-frequency fluctuations from the signals. Test condition details: new model rotor experiments under controlled conditions (New MEXICO) data point 407; β = −90°; U_∞=30 m/s; θ= 90.0°; Ω=0.0 rpm [Colour figure can be viewed at wileyonlinelibrary.com]

$$F_t = \sum_{i=1}^{N} \frac{1}{2}(p_i + p_{i+1})(y_i - y_{i+1}). \tag{2}$$

In the above equation, values of variables for (N+1)*th* subscript are taken to be equal to the fictitious pressure tap with subscript 1. F_n and F_t represent normal and tangential force, respectively, while p denotes pressure. An example of computed normal and tangential force time signal for one particular data point is presented in Figure 2.

3 | RESULTS AND DISCUSSION

3.1 | 3D airfoil polars

In this section, the standstill measurements in the New MEXICO database are used to recreate the steady 3D airfoil polars. The purpose of doing this exercise is to compare the results with 2D airfoils polars and the trends observed in the literature to verify the measurements. A summary of all the standstill data points used for this recreation are outlined in Table 1. Each data point would correspond to one point on the C_l versus α and C_d versus α curve for a particular spanwise section. The AoA corresponding to each C_l and C_d value is computed through geometric considerations as presented in Figure 3. It is to be noted that assuming a pure geometric AoA is an approximation, and in reality, induction effects due to downwash are expected to result in a slightly lower effective AoA. However, the scale of these inductions effects is assumed to be small. Standstill cases with yaw where the blade section is either at 8 o' clock or 4 o' clock position have been excluded in this extraction process because of strong spanwise flow components in those blade positions. However, standstill cases with yaw where the blade is at the 12 o' clock position are included while recreating 3D airfoil polars.

The standstill cases in axial flow and yawed flow with zigzag tape on outboard part of blade ($\frac{r}{R} > 0.7$) covered a wider range of AoA in comparison with axial flow without zigzag tape; therefore, it is presented in Figure 4. In this figure, there is an increase in unsteadiness after stall indicated by the increasing standard deviation in the lift force coefficient. Furthermore, an increase in the standard deviation of the drag coefficient with a subsequent decrease in the standard deviation of lift coefficient is observed in the deep stall regime beyond, approximately, 50° AoA. This is expected as the airflow nearly becomes perpendicular to the airfoil and lift coefficient approaches almost zero. A similar sort of trend in standard deviation is also observed for deep stall with negative AoA. However, in this case, the location of stall is not clearly indicated because of the lack of sufficient data points.

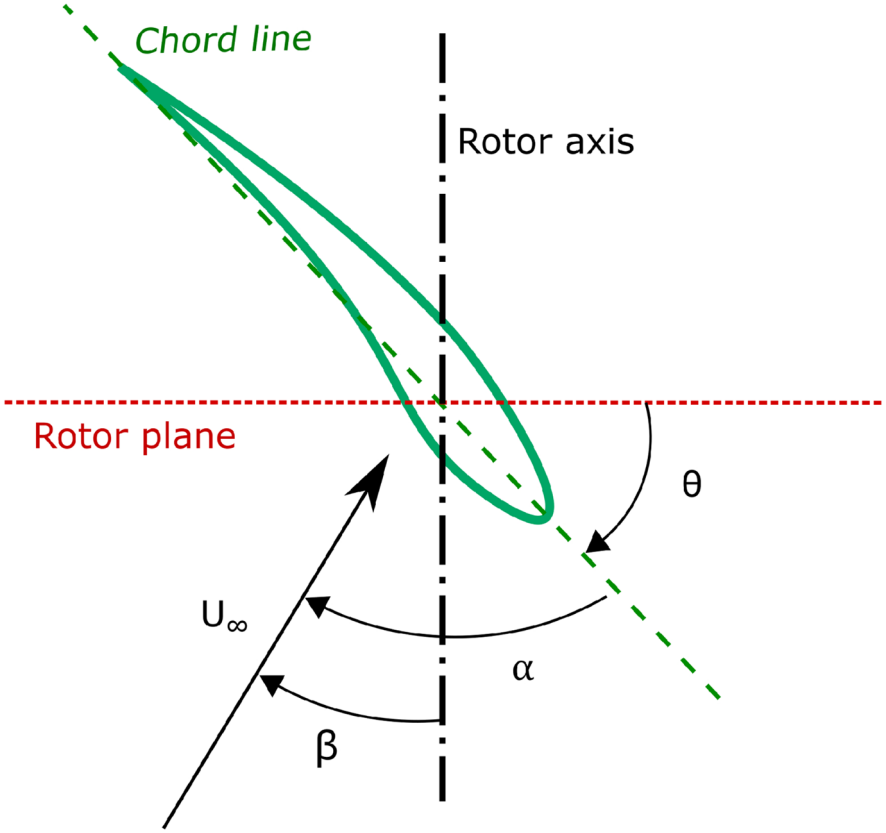

FIGURE 3 Schematic showing the calculation of geometric angle of attack (AoA) for standstill cases with yaw. Note: the geometric AoA is only calculated for 12 o' clock blade position [Colour figure can be viewed at wileyonlinelibrary.com]

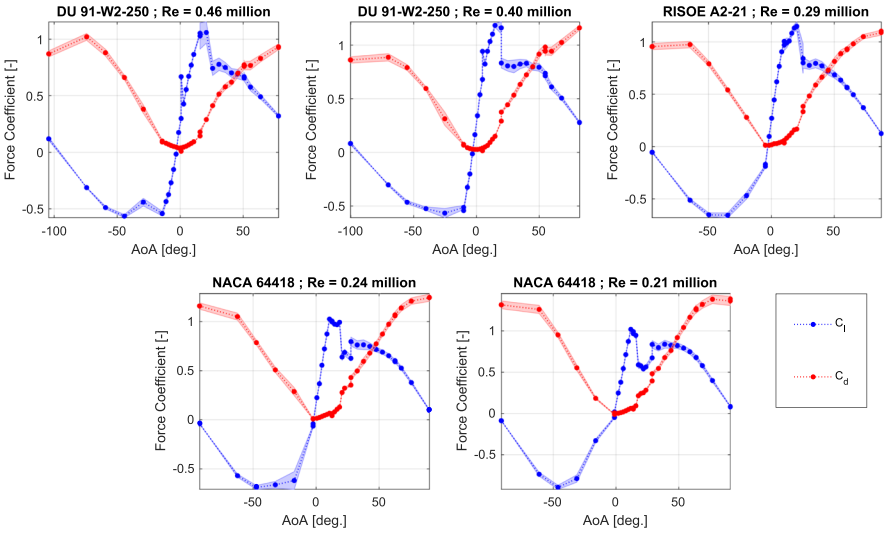

FIGURE 4 Airfoil polars reconstructed from the new model rotor experiments under controlled conditions (New MEXICO) standstill measurements in axial and yawed conditions with zigzag tape installed on outboard blade sections ($\frac{r}{R}$ > 70%). The angle of attack (AoA) on the x-axis is the geometric AoA and the tunnel velocity in all these test runs was approximately 30 m/s. Note: the shaded regions denote the standard deviation of the measurements [Colour figure can be viewed at wileyonlinelibrary.com]

3.1.1 | Comparison with 2D airfoil polars

The agreement of the 3D airfoil polars with the 2D airfoil polars, available from wind tunnel experiments,[12,20,21] is reasonably good within attached flow regime and up until stall. However, in the deep stall regime, there is a large difference between the airfoil polars. This is expected as a 2D section has more base drag in comparison with a 3D section. It is to be noted that the 2D airfoil polars in deep stall regime, for all three airfoil sections, are taken from deep stall measurements on DU96-W-180 airfoil conducted by TU Delft.[22] This was done because of non-availability of wind tunnel data for those airfoils at very large AoA. It is to be mentioned that a major difference between the 2D and 3D airfoil polars is that the latter do not have viscous effects because New MEXICO did not have provision for a wake rake to measure viscous drag effects. Therefore, the viscous drag representation from 3D polars is expected to be inaccurate below stall. Lindenburg[23] assumed the influence of

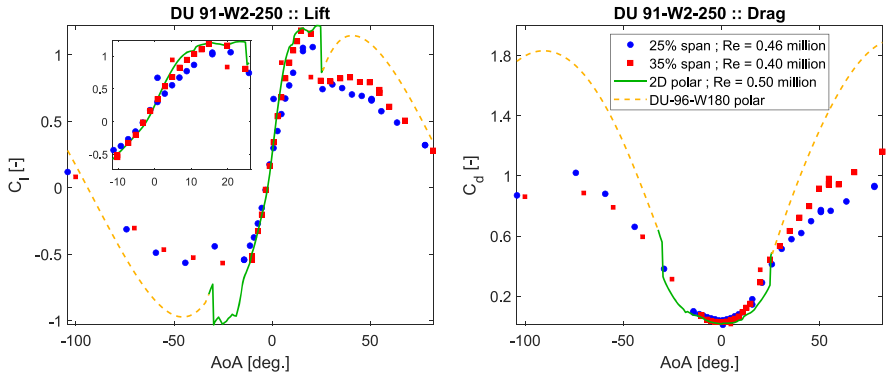

FIGURE 5 Comparison between blade section airfoil polars extracted from standstill measurements (shown as red or blue points) with the respective 2D airfoil polars (green curve) [Colour figure can be viewed at wileyonlinelibrary.com]

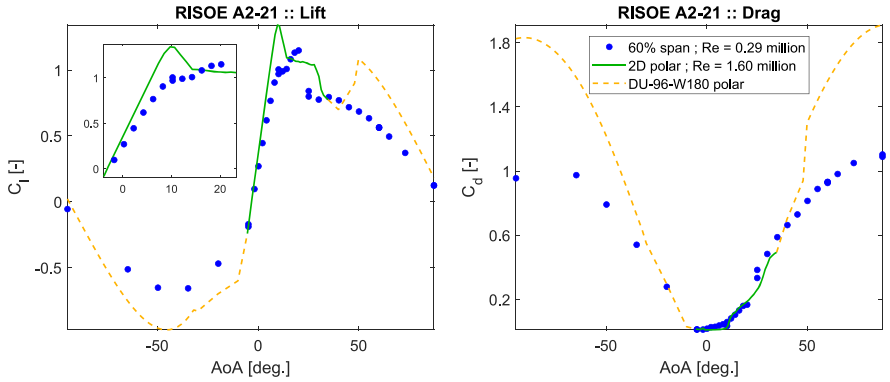

FIGURE 6 Comparison between blade section airfoil polars extracted from standstill measurements (shown as blue points) with the respective 2D airfoil polars (green curve) [Colour figure can be viewed at wileyonlinelibrary.com]

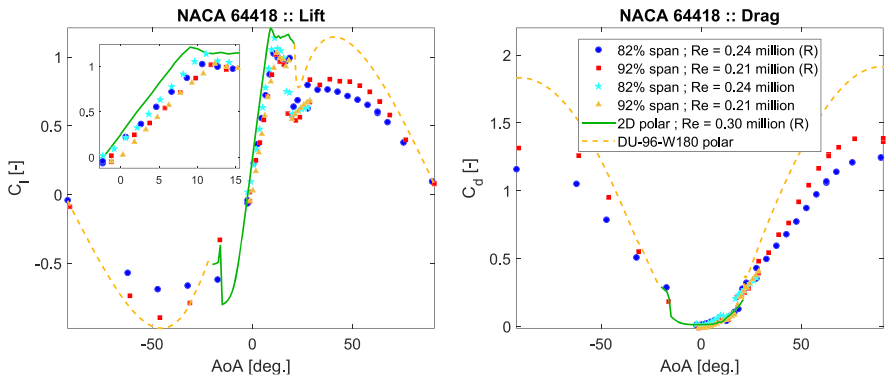

FIGURE 7 Comparison between blade section airfoil polars extracted from standstill measurements (shown as red or blue points) with the respective 2D airfoil polars (green curve). Note: (R) denotes outboard roughness installed or outboard roughness effects are included [Colour figure can be viewed at wileyonlinelibrary.com]

Reynolds number in the deep stall regime to be minimal for wind turbine applications. This assumption is somewhat true as, typically, high Reynolds number delays separation by transitioning the boundary layer to turbulent or by energizing the boundary layer. However, for complete separation in deep stall regime, this might not be the case. The Reynolds number for the DU 91-W2-250 airfoil section in Figure 5 is almost similar between the 2D and 3D airfoil polars. In the case of RISØ A2-21 section, the 2D airfoil polar is for a very high Reynolds number compared with the 3D polar, which could be the reason for the higher $C_{l_{max}}$ observed for 2D airfoil polar in Figure 6. Furthermore, it should be noted that the 2D airfoil data shown here for RISØ A2-21 is actually for RISØ A1-21, as indicated by Boorsma and Schepers.[12] Finally, for the NACA 64418 section, the Reynolds numbers between 2D and 3D airfoil polars are comparable. However, it is to be noted that this blade section, containing NACA airfoil sections, would only experience these low Reynolds numbers in standstill conditions. In normal operations, this section would experience Reynolds numbers close to 0.7 million.

Observing Figure 5, it can be seen that the lift coefficient for the section closer to the root is lower than the lift coefficient for 35% section and 2D airfoil polar. This is due to induction effects from the root of a finite aspect ratio MEXICO blade. A similar behavior was reported by Timmer[24] for the NREL UAE phase VI measurements in NASA Ames wind tunnel. There, he also observed that these end effects due to induction were more visible for sections closer to the root. On the other hand, in Figure 7, despite the fact that the lift coefficient curves of the NACA airfoil closer to the tip have the lowest lift gradient in attached flow, unlike the DU-airfoil, they have a higher lift and drag coefficient in deep stall regime compared with the section at 82%.

3.1.2 | Comparison with flat plate theory in deep stall

In the deep stall regime, flow over the upper airfoil surface is completely separated. In such a situation, the influence of upper surface thickness on pressure distribution is negligible, for airfoils with moderate lower surface thickness, as was pointed out by Timmer[24] and Lindenburg.[25] On this basis, it can be assumed that the lift to drag ratio in the deep stall regime would closely resemble that of a flat plate as the upper surface pressure distribution is independent of upper surface thickness. The lift and drag coefficient can be computed from the following equation on the basis of ideal flat plate theory, taken from Timmer[24]:

$$C_l = 2\sin\alpha\cos\alpha, \tag{3}$$

$$C_d = 2\sin^2\alpha. \tag{4}$$

Using the above equations, lift to drag ratio for an ideal flat plate was computed and plotted against the lift to drag ratio obtained from 3D and 2D airfoil polars in Figure 8A. In this figure, it is seen that all curves coalesce to follow the trend predicted by flat plate theory above 30° AoA, characterizing deep stall regime. However, below this AoA, lift to drag ratio differ depending upon the airfoil section and the spanwise location. It is to be mentioned here that 2D airfoil polars in the deep stall regime are taken from the DU-96-W180 profile.[22] Data at moderate AoA is

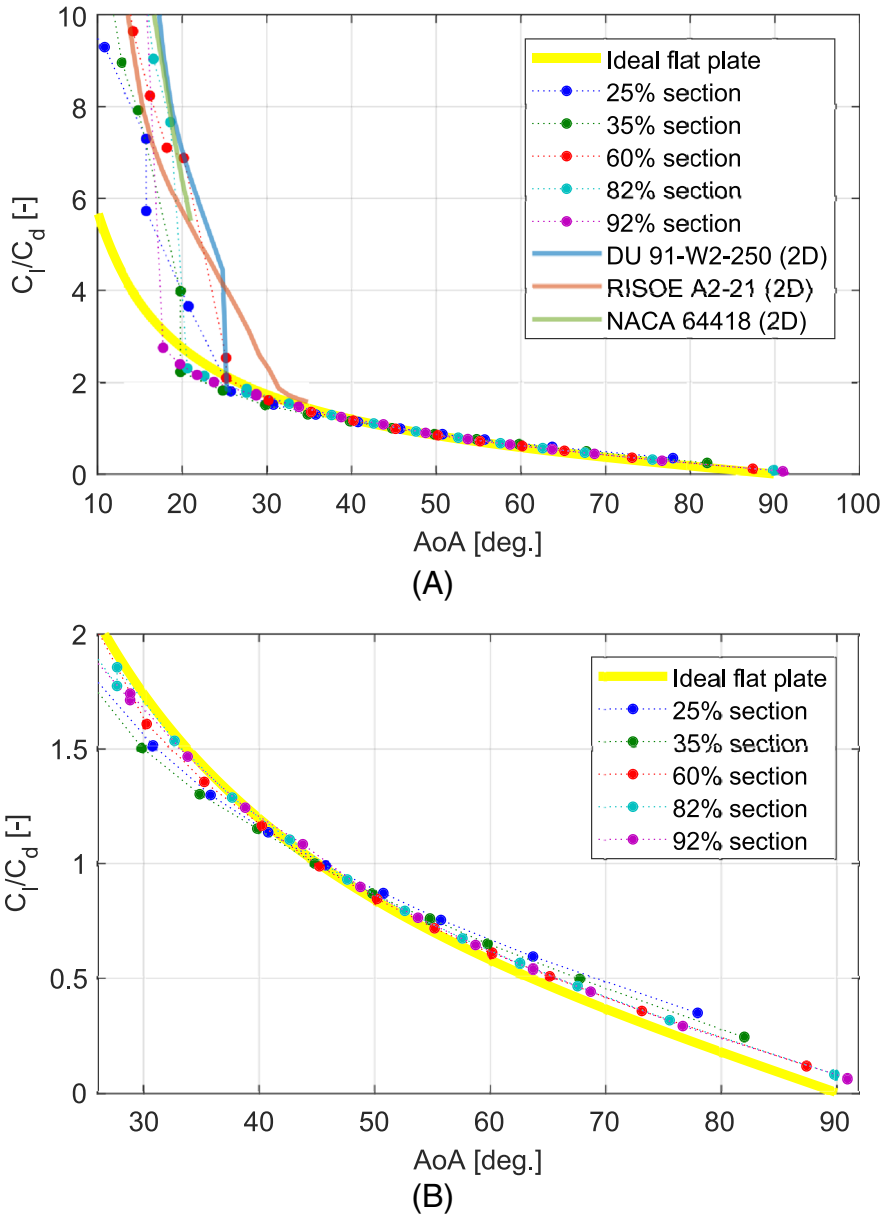

FIGURE 8 Lift to drag ratio versus angle of attack (AoA) for the new model rotor experiments under controlled conditions (New MEXICO) blade sections. A, A comparison of lift to drag ratio of 3D polars from five different sections of New MEXICO blade with the ideal flat plate theory and 2D airfoil polars. B, A close-up of Figure 8A in the deep stall regime [Colour figure can be viewed at wileyonlinelibrary.com]

obtained from experimental measurements on the respective airfoils, and in Figure 8A, the 2D polars are shown up till these AoA (excluding DU-96-W180 data in deep stall). For the 2D polars, the deep stall regime starts above 30° for the RISØ airfoil section, while for the DU airfoil section, it starts above 25°. Because of the lack of data for the NACA airfoil in deep stall, it is hard to pinpoint at which AoA the deep stall regime would start; however, on the basis of visual inspection, it seems to be lower than 25°. For the 3D polars, the 25% and 35% DU profile sections and the 60% RISØ profile section have a higher relative thickness than the NACA profile at the 82% and the 92% sections. It appears that the 3D polars for the DU and the RISØ profile sections (ie, 25%, 35%, and 60% sections) seem to enter deep stall regime at a relatively higher angle of attack than the NACA profile sections (ie, 82% and 92% section). This behavior could be because relatively thinner airfoils show a tendency of leading edge separation with large separation over the complete upper surface, often referred to as "thin airfoil stall,"[26] similar to a flat plate where onset of leading edge separation causes an abrupt stall. Because of this tendency, relatively thin airfoils seem to enter deep stall at lower AoA. However, Timmer and Van Rooij[20] have argued that it is not the airfoil thickness but the leading edge thickness that is more important to the deep stall angle. A peculiar behavior of the RISØ profile section is that despite having a lower maximum relative thickness of 21% compared with the DU profile section's 25% maximum relative thickness, it seems to enter deep stall (or, in other words, onset of leading edge separation) at a relatively higher AoA for both 2D and 3D airfoil polars. Compared with the DU profile, the RISØ profile has a large camber because of a comparatively lower lower surface thickness. To sum up, Figure 8A further confirms an already know fact, presented by Timmer,[24] that the lift to drag ratio for a finite or infinite (2D) blade section is identical to that of a flat plate, thus strengthening the credibility of New MEXICO measurements in standstill conditions.

3.2 | Frequency domain analysis

In this section, a frequency domain analysis of the New MEXICO measurements in standstill conditions is presented. The main purpose of undertaking this campaign was to unmask vortex shedding of self-excited nature. Before performing the frequency domain analysis, time series data were inspected. In this case, times series of normal and tangential force is obtained from integrating differential pressures from pressure ports, discussed in Section 2.1.2. A time series of such a data for a particular spanwise location and test condition is presented in Figure 2. Here, the time series has also been filtered, using a low pass infinite impulse response (IIR) filter with a passband frequency of 40 Hz, to visualize any cyclic behavior in the signal. The time signal shows repetition of peaks in time, but it is hard to imply anything about the periodicity of signal or its frequency content. Therefore, a Fourier analysis is justified.

3.2.1 | Signal processing

In the New MEXICO test runs, pressure data was acquired for approximately 5 seconds at a frequency of 5514 Hz, giving a total of 27 610 sample points for each run. This gives a frequency resolution of $\frac{5514}{27610} \approx 0.2$ Hz in the frequency domain. Before performing spectral analysis, some preprocessing of the signal was carried out. The normal and tangential force signals were subtracted from their mean values (here, assuming stationary time series or assuming that the mean does not change in time as test conditions don't change) to remove power of DC frequency. Otherwise, the spectrum would give huge peaks at zero frequency as it contains most of the signal energy. Additionally, signals were divided by their standard deviation to standardize the spectrum output and facilitate comparison between normal and tangential force spectrum on the same plot, as they are of different orders of magnitude. The standardization process in mathematical notation is expressed as

$$Z(t) = \frac{X(t) - \bar{X}}{\sigma_X}, \tag{5}$$

where $X(t)$ is the time series signal, $\bar{X}$ is the mean, and σ_X is the standard deviation of that signal. $Z(t)$ is the standardized signal. After standardization, Welch's method was used in MATLAB to estimate the power spectral density of signals. Shaping of the signal, through the use of windowing functions, was also performed to mitigate noise in the spectrum by averaging segments (windows) of the time series and also reducing spectral leakage in the process. It is to be noted that a smaller window size results in more averaging of segments. A comparison of its effects is presented in Figure 9 for a "hanning" window function with 50% overlap. A window size of 4000 implies that the signal has been divided into approximately six segments containing 4000 samples each. In Figure 9A, windowing has reduced noise in the spectrum but at the cost of increasing frequency bin resolution to approximately 1.38 Hz. Moreover, the windowing function does not uncover or unmask dominant frequency peaks, which are not visible from a spectrum with a window size equal to total number of signal samples (27610), as shown in Figure 9B, which has a better frequency resolution of 0.2 Hz. Hence, the latter windowing function setting was chosen for subsequent analysis.

In order to identify erroneous frequency components, spectra of test runs with zero tunnel speed before and after axial and yawed flow standstill runs were analyzed. Certain peaks in power spectral density (PSD) were observed at frequencies to which no definite cause could be associated, as highlighted by the red circles in Figure 10B, corresponding to 0.1997 and 12.78 Hz. Figure 10A shows that there is some noise in all pressure sensor signals at zero tunnel speed. The erroneous frequencies are either due to malfunctioning pressure sensors or some external

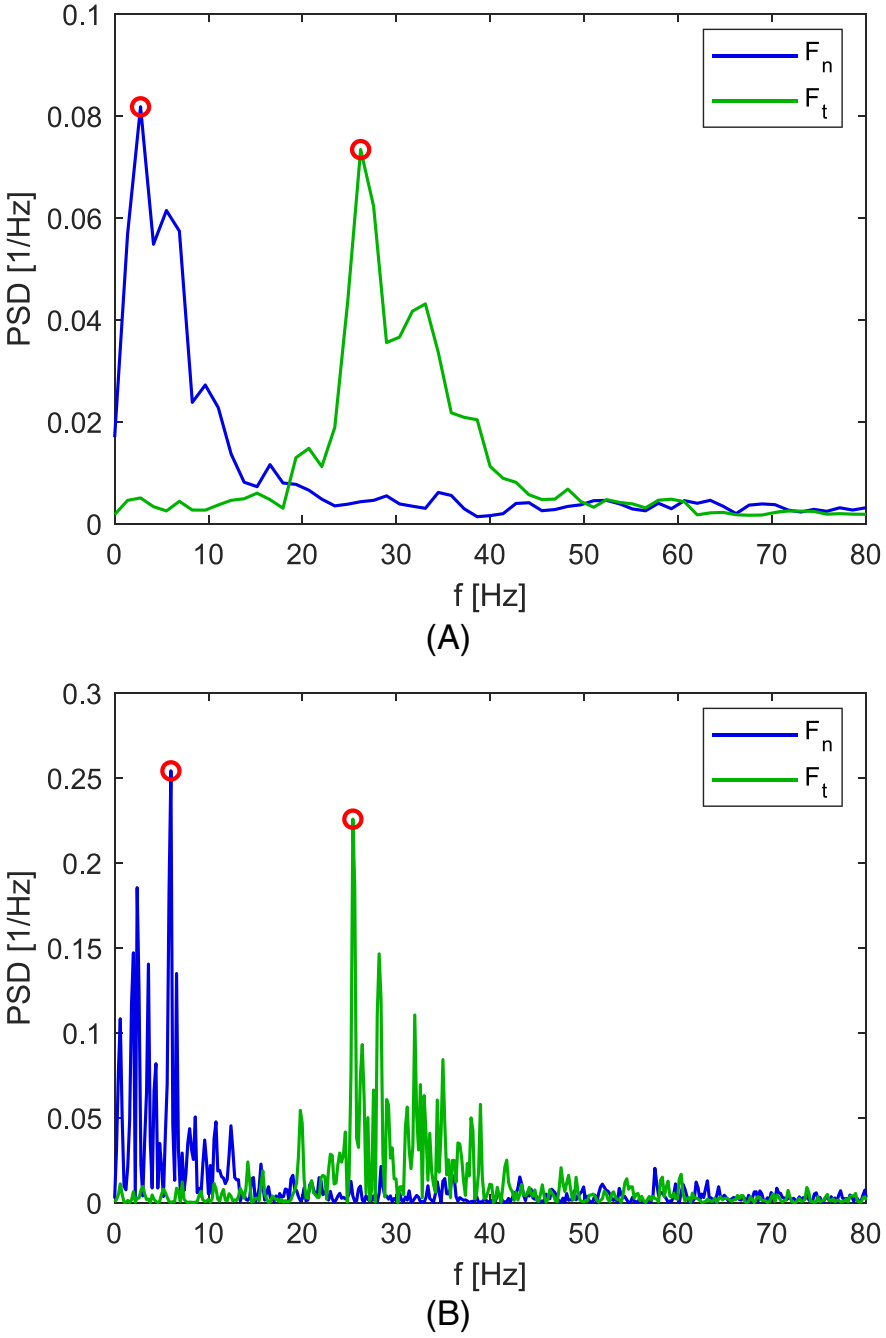

FIGURE 9 Power spectral density (PSD) plot showing the frequency (f) content of normal force and tangential force time signal for two different window sizes. The spectra is show for 82% spanwise section with the following test conditions: Data point 407 ; β=−90° ; U_∞=30m/s ; θ=90.0°; Ω=0.0 rpm [Colour figure can be viewed at wileyonlinelibrary.com]

disturbance source. It is highly likely that these frequencies are from malfunctioning pressure sensors. Most of these erroneous frequencies are also observed for cases with tunnel speed of 30 m/s, suggesting that the spectral power of these frequencies is increased with tunnel speed to make them standout among other flow-related frequency content, which could only be possible if they are from malfunctioning pressure sensors. This is because if they were from an external disturbance source, then their power content would have been relatively lower than other flow mechanisms at higher tunnel speeds. A summary of all observed erroneous frequencies in test runs at zero tunnel speed is presented in Table 3.

3.2.2 | Strouhal number

The process of dominant frequency extraction was automated in MATLAB environment to evaluate the frequency content across all the varied standstill test conditions. A scatter plot of dominant frequencies extracted from all standstill runs and spanwise sections is presented in Figure 11, where they are plotted against the corresponding geometric AoA. The figure contains dominant frequencies from both normal and tangential force time signals in one plot. Most of the frequencies observed below the 15-Hz level (shown by dashed black line in Figure 11) will be discarded

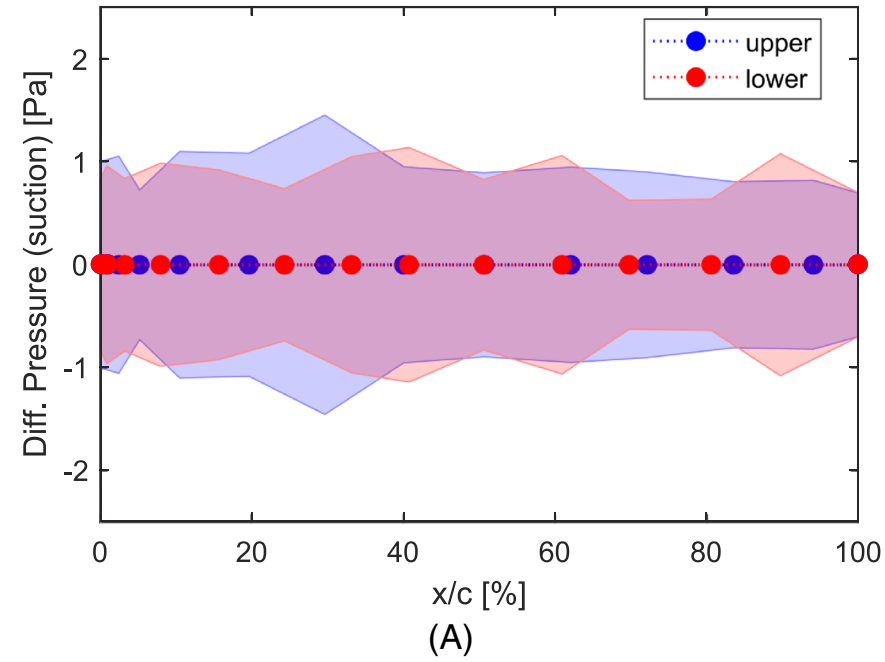

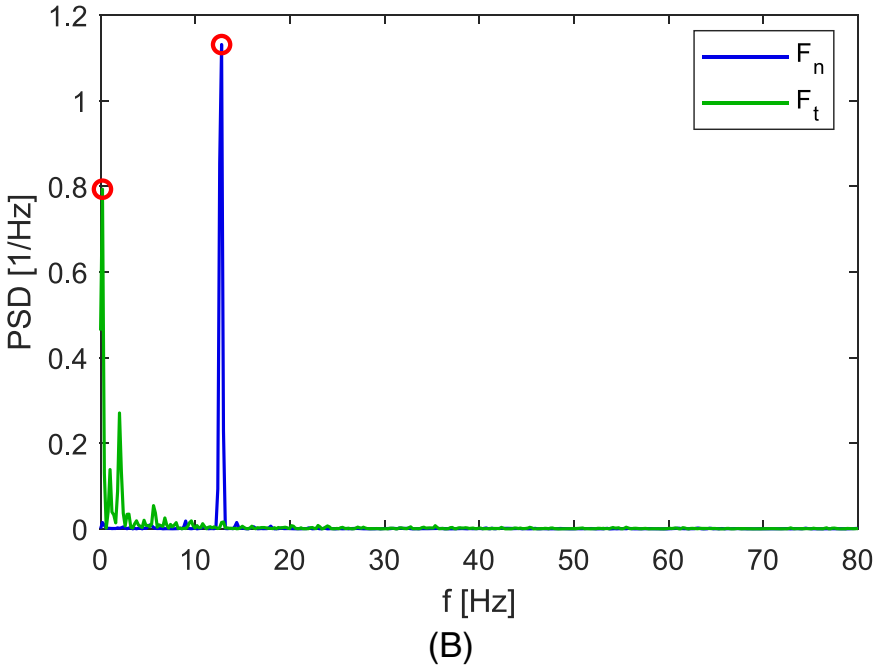

FIGURE 10 Pressure port signals and power spectral density (PSD) of normal and tangential force signal for test case at zero tunnel speed. The results are shown for 35% spanwise section with the following test conditions: Data point 371 ; β=0° ; U_∞=0 m/s; θ=0°; Ω=0.0 rpm [Colour figure can be viewed at wileyonlinelibrary.com]

TABLE 3 A compilation of erroneous frequencies observed in standstill runs at zero tunnel speed (U_∞=0 m/s)

Case Type	Data Point	β, degree	θ, degree	Erroneous Frequencies, Hz
Axial flow[a]	371	0	0	0.1997, 0.3994, 12.58, 12.78
	396	0	25	0.1997, 0.7988, 3.195, 11.58
	402	0	−2.3	0.1997, 0.9986, 12.78
Yawed flow[a]	404	−90	90	0.1997
	426	0	90	0.1997, 0.3994

[a]With outboard roughness installed on New MEXICO rotor.

while computing the Strouhal number because of two main reasons: Firstly, the frequencies below this level correspond to erroneous frequencies listed in Table 3, and secondly, these frequencies would result in very low Strouhal numbers that cannot be associated with any flow mechanism. Therefore, with an aim of avoiding ambiguity, frequencies below 15-Hz level have been filtered out while computing the Strouhal number. The

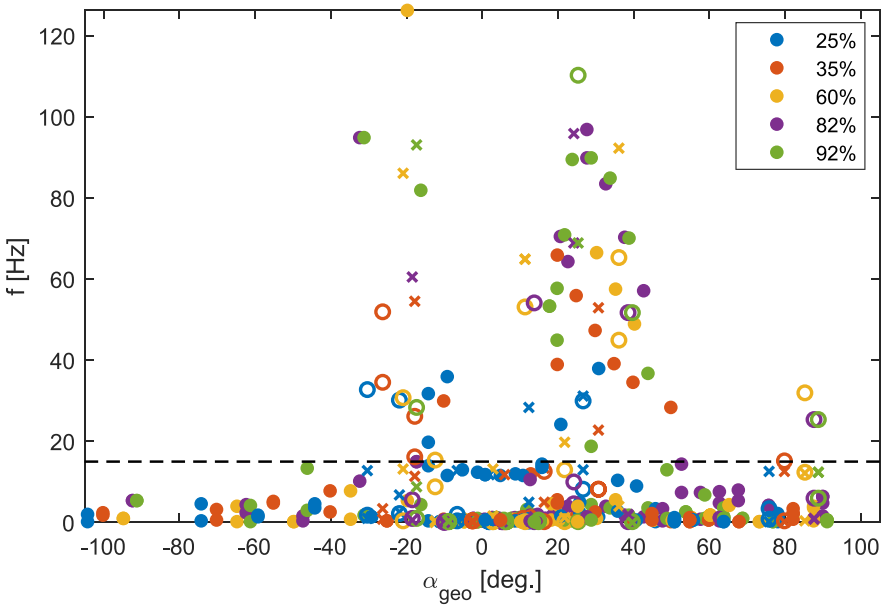

FIGURE 11 Scatter plot showing dominant frequencies observed in all standstill cases versus the corresponding geometric angle of attack (AoA) (α_{geo}) at a particular test condition and spanwise location. The cross markers (**x**) denote presence of spanwise flow from tip to root, hollow circle markers (**o**) denotes presence of spanwise flow from root to tip, and filled circle markers (•) represent no spanwise flow. The dashed black line denotes the 15-Hz frequency level [Colour figure can be viewed at wileyonlinelibrary.com]

Strouhal number is computed according to the following formula:

$$St = \frac{fL_{char}}{V}, \tag{6}$$

where, L_{char} is the characteristic length based on the projected chord length or airfoil section thickness t perpendicular to the incoming flow and is equal to

$$L_{char} = \max\begin{cases} c\sin\alpha, \\ t. \end{cases} \tag{7}$$

V is the local inflow velocity in the plane of a blade section, and f is the principle shedding frequency. A scatter plot of Strouhal frequencies observed in standstill conditions is presented in Figure 12. Firstly, only the solid circle markers are discussed. This figure shows two distinct clusters of data points—one in the positive AoA range from approximately 16° to 42° and another cluster from −9° to −32°. A denser clustering of data points highlighted by the solid black curve lies in the Strouhal number range of 0.12 to 0.20, which is typical for bluff body vortex shedding in deep stall as was mentioned by Schreck.[27] These Strouhal numbers occur between 20° and 50° in deep stall regime for the New MEXICO blade. It can be seen, depending on the blade section, that the Strouhal number remains almost constant for a small range of AoA within this region, especially prominent for the 35% blade section. In the literature, there have been numerous experimental and computational studies to determine bluff body vortex shedding Strouhal number. Yang et al[28] mentioned experiments conducted by Fage and Johansen[29] on inclined flat plates where they

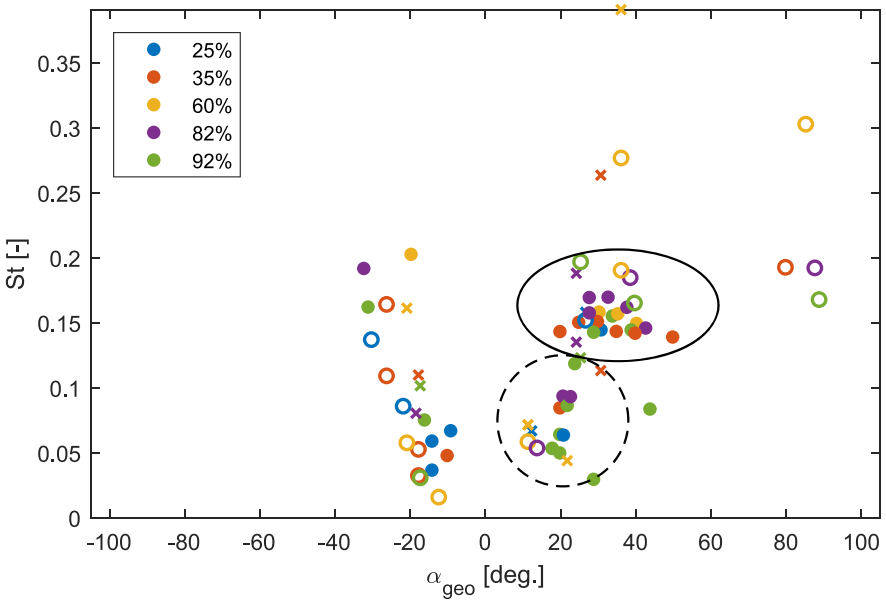

FIGURE 12 Scatter plot showing Strouhal numbers observed in all standstill cases versus the corresponding geometric angle of attack (AoA) (α_{geo}) at a particular test condition and spanwise location. The cross markers (**x**) denote presence of spanwise flow from tip to root, hollow circle markers (**o**) denotes presence of spanwise flow from root to tip, and filled circle markers (•) represent no spanwise flow [Colour figure can be viewed at wileyonlinelibrary.com]

TABLE 4 A summary of Strouhal frequencies observed for near-stall flow oscillations on airfoils in the literature

Source	Strouhal number [-]
Zamman et al[36,38]	~0.02
Mabey[37]	0.076
Bragg et al[34]	0.017-0.032
Yon and Katz[35]	0.04-0.06
Schreck[27]	0.01-0.08
Present study	0.04-0.10

found an approximately constant Strouhal number of 0.148 for 30° to 90° AoA (Reynolds number in this study is not explicitly mentioned, but according to a rough estimation, it is about 0.17 million). Yang et al[28] themselves did a DNS simulation, but it was for a very low Re, and AoA is up till 30°. Another important aspect of the effect of the shape of a bluff body on the Strouhal number was highlighted by Radi et al.[30] Although their study was also at very low Reynolds number, they did show that the Strouhal number changed from 0.2 to 0.155 for a perfect circular cross-section to a flat plate cross-section, respectively, signifying the effect of cross-sectional shape on Strouhal number. Analysis of wind tunnel tests on wind turbine airfoil section (S809 airfoil) at high AoA by Swalwell[31] revealed Strouhal numbers from 0.15 to 0.18. Pellegrino and Meskell[32] conducted a computational study on the same airfoil section at very high AoA, revealing Strouhal numbers from 0.11 to 0.15, close to that of a flat plate. Lastly, Boorsma[33] performed a wind tunnel investigation on the DU91-W2-250 profile at large AoA, the same as the inboard airfoil section of the MEXICO blade, and found Strouhal numbers from 0.16 to 0.17.

Another important aspect in Figure 12 is highlighted by the dashed black curve. Here, the points represent a post-stall periodic flow regime. This "low-frequency" (low Strouhal number) oscillatory flow regime near stall has been observed in the past by Schreck,[27] Bragg et al,[34] Yon and Katz,[35] Zaman et al,[36] and Mabey.[37] Zaman et al[38] first documented this low-frequency flow oscillation with a Strouhal number of 0.02 (Re=4×10^4 – 1.4×10^5) on a LRN (1)-1007 airfoil. They later conducted experimental and computational studies[36] to further investigate the phenomena. There, they traced the origin of these low-frequency oscillations near the leading edge of the airfoil upper surface to "periodic switching between stalled and unstalled states." Bragg et al[34] conducted further experiments on LRN(1)-1007 airfoil at various Reynolds numbers and AoA. They found, in general, that the Strouhal number in the low-frequency regime increases with AoA and Reynolds number. Through laser sheet and surface oil flow visualization, they were able to relate the cause of these oscillations to a leading edge separation bubble. They concluded that formation and bursting of the leading edge separation bubble is what causes the low-frequency oscillations. A summary of the Strouhal numbers associated with the low frequency oscillations near stall observed in various studies is presented in Table 4. For the New MEXICO blade, the low-frequency region lies between approximately 15° and 22° AoA, which is in fact close to the near- or post-stall region of the airfoil sections. The Strouhal numbers within this region range from 0.05 to 0.09.

In Figure 12, hollow circle markers represent spanwise flow from root to tip, while cross markers represent spanwise flow from tip to root at a blade section. These markers are more dispersed over the domain of interest. It is hard to associate any peculiar trend to these marker points. A 3D CFD simulation is needed to accurately predict and verify the behavior at these marker points.

Generally, for the New MEXICO blade, periodic bluff body vortex shedding is seen for a small AoA range in the deep stall regime. It is nearly non-existent for AoA beyond 50°. This behavior could be due to the finite aspect ratio effects. Lindenburg[25] hypothesized that an infinitely long rectangular flat plate is more probable to have structured vortex shedding than a finite aspect ratio flat plate. His hypothesis was based on experiments conducted on airfoils with and without end plates.[39,40] Therefore, a finite aspect ratio blade (the New MEXICO blade has an aspect ratio of 14) will have partially structured vortex shedding due to early break-up of shed vortices caused by suction of air into the vortex core. Lindenburg[25] also associated the absence of periodic vortex shedding in a finite aspect ratio blade to the lower drag coefficient at AoA close to 90°. In case of New MEXICO blade, this effect is clearly visible from 3D airfoil polars in Figures 5 to 7.

4 | CONCLUSIONS

A frequency domain analysis was performed on the New MEXICO standstill measurements. As a priori, 3D airfoil polars were recreated from standstill measurements and compared against 2D airfoil polars. Furthermore, lift to drag ratio variation with AoA, obtained from 3D airfoil polars, was compared with flat plate theory results to verify the measurements. Spectral analysis was performed on time series data computed from pressure measurements on the New MEXICO rotor in standstill conditions. Dominant shedding frequencies were revealed for certain ranges of geometric AoA. Two dominant shedding modes were identified, namely, a bluff body vortex shedding mode and a low Strouhal number shedding mode. The following main conclusions were drawn from the current research.

A reasonable agreement was found between the 2D and 3D airfoil polars in the attached flow regime up to stall. An exception to this rule was the RISØ airfoil at 60% spanwise section, which showed different stall behavior than its 2D airfoil polar. However, in deep stall, the 3D airfoil polars

showed lower lift and drag coefficients than the 2D airfoil polars. The lift to drag ratio versus AoA trend obtained from 3D airfoil polars matches well with the trend predicted by 2D flat plate theory in the deep stall regime. This is because in deep stall, the flow is completely separated over the upper surface, and the effect of upper surface thickness can be neglected. The relatively thin NACA airfoil profile enters deep stall earlier than the DU and the RISØ airfoil profile because of higher tendency towards leading edge separation because of its relatively lower thickness.

Structured bluff body vortex shedding was observed in a limited range of AoA from 20° to 50° in the deep stall regime on the New MEXICO blade. The 35% section on the New MEXICO blade showed bluff body vortex shedding for a wider range of AoA than the 25% section, possibly because of tip losses near the root section. The bluff body vortex shedding Strouhal numbers were seen to lie between 0.13 and 0.2. Low Strouhal number shedding behavior was observed in the post stall regime, and the Strouhal number was seen to increase with increasing AoA. The absence of structured vortex shedding at very large AoA was attributed to finite aspect ratio of the MEXICO blade, which destabilizes the vortex core causing early break-up of shed vortices.

This research is another step forward to comprehend the complex flow physics of the deep stall regime. However, further research is needed to completely understand the complex underlying flow physics in the stall regime.

ACKNOWLEDGEMENTS

The authors would like to acknowledge Koen Boorsma for providing access to the New MEXICO measurements. The research was supported by Energy Research Center of the Netherlands, now part of Netherlands Organization for Applied Scientific Research.

ORCID

Muhammad A. Khan https://orcid.org/0000-0002-4845-2132

REFERENCES

1. Hansen MH. Aeroelastic instability problems for wind turbines. *Wind Energy*. 2007;10(6):551-577.
2. Heinz JC, Sørensen NN, Zahle F, Skrypinski W. Vortex-induced vibrations on a modern wind turbine blade. *Wind Energy*. 2016;19(11):2041-2051.
3. Zou F, Riziotis VA, Voutsinas SG, Wang J. Analysis of vortex-induced and stall-induced vibrations at standstill conditions using a free wake aerodynamic code. *Wind Energy*. 2015;18(12):2145-2169.
4. Skrzypiński W, Gaunaa M, Heinz J. Modelling of vortex-induced loading on a single-blade installation setup. *J Phys Conf Ser*. 2016;753(8).
5. Heinz JC, Sørensen NN, Zahle F. Fluid-structure interaction computations for geometrically resolved rotor simulations using CFD; 2016.
6. Larsen TJ. How 2 HAWC2, the user's manual, Technical Report R-1597(EN), Technical University of Denmark; 2009.
7. Michelsen JA. Block structured multigrid solution of 2D and 3D elliptic PDE's; 1994.
8. Sørensen NN. General purpose flow solver applied to flow over hills. *Ph.D. Thesis*; 1995. https://findit.dtu.dk/en/catalog/2389468882
9. Snel H. Heuristic modelling of dynamic stall characteristics. In: EWEC conference. Bookshop for Scientific Publications; 1997:429-433.
10. Bertagnolio F, Sørensen NN, Rasmussen F, Johansen J, Madsen HA. A stochastic static stall model applied to a wind turbine blade. *AIAA Applied Aerodynamics Conference*. 2008:1-18.
11. Bertagnolio F, Rasmussen F, Sorensen NN, Johansen J, Madsen HAa. A stochastic model for the simulation of wind turbine blades in static stall. *Wind Energy*. 2010;13(4):323-338.
12. Boorsma K, Schepers G. Description of Experimental Setup: New MEXICO experiment. ECN; 2017.
13. Schepers JG, Boorsma K, Cho T, other. Final report of IEA Task 29, Mexnext (Phase 1): Analysis of MEXICO wind tunnel measurements; 2012.
14. Schepers JG, Boorsma K, Gomez-Iradi S, other. Final report of IEA Task 29. Mexnext (Phase 2), Researchgate.Net; 2014. http://www.researchgate.net/profile/Daniel_Micallef/publication/272183785_Final_report_of_IEA_Task_29_Mexnext_(Phase_1)_Analysis_of_Mexico_wind_tunnel_measurements/links/54df3a550cf2953c22b16a4d.pdf
15. Boorsma K, Schepers JG, Gomez-Iradi S, other. Final report of IEA Wind Task 29 Mexnext (Phase 3), ECN part of TNO; 2018.
16. Parra EA. Data reduction and analysis of New MEXICO experiment; 2016.
17. Khan MA. Dynamic stall modeling for wind turbines. *Master Thesis*; 2018.
18. Boorsma K, Schepers JG. New MEXICO experiment: preliminary overview with initial validation, ECN; 2014.
19. Schepers JG, Snel H. Model experiments in controlled conditions—final report. ECN Report: ECN-E-07-042; 2007.
20. Timmer WA, van Rooij RPJOM. Summary of the Delft University wind turbine dedicated airfoils. *J Sol Energy Eng*. 2003;125(4):488. http://solarenergyengineering.asmedigitalcollection.asme.org/article.aspx?articleid=1456892
21. Fuglsang P, Bak C. Development of the Risø wind turbine airfoils. *Wind Energy*. 2004;7(2):145-162. http://doi.wiley.com/10.1002/we.117
22. Timmer W, Rooij RV. Some aspects of high angle-of-attack flow on airfoils for wind turbine application. *EWEC 2001, Copenhagen, Denmark*. 2001;2015:4-7. http://www.lr.tudelft.nl/fileadmin/Faculteit/LR/Organisatie/Afdelingen_en_Leerstoelen/Afdeling_AEWE/Wind_Energy/Research/Publications/Publications_2001/doc/TimmerEWEC2001.pdf
23. Lindenburg C. Aerodynamic airfoil coefficients at large angles of attack. *Annual IEA Symposyum on the Aerodynamics of Wind Turbines*; 2000:1-18.

24. Timmer WA. Aerodynamic characteristics of wind turbine blade airfoils at high angles-of-attack. *TORQUE 2010: The Science of Making Torque from Wind*; 2010:71-78.
25. Lindenburg C. Investigation into rotor blade aerodynamics analysis of the stationary measurements on the UAE phase-VI rotor in the NASA-Ames wind tunnel. *Ecnnl*. 2003;July:114. http://www.ecn.nl/docs/library/report/2003/c03025.pdf
26. Anderson Jr JD. *Fundamentals of Aerodynamics*. Fifth, Vol. Fifth edit; 2011.
27. Schreck S. Spectral content and spatial scales in unsteady rotationally augmented flow fields. *J Phys Conf Ser*. 2007;75(1).
28. Yang D, Pettersen B, Andersson HI, Narasimhamurthy VD. Vortex shedding in flow past an inclined flat plate at high incidence. 2012.
29. Fage A, Johansen FC. On the flow of air behind an inclined flat plate of infinite span. 1927:170-197. http://rspa.royalsocietypublishing.org/cgi/doi/10.1098/rspa.1927.0130
30. Radi A, Thompson MC, Sheridan J, Hourigan K. From the circular cylinder to the flat plate wake: the variation of Strouhal number with Reynolds number for elliptical cylinders; 2013.
31. Swalwell KE. The effect of turbulence on stall of horizontal axis wind turbines. BSc Monash University. 2005:1-307. http://scholar.google.com/scholar?hl=en&btnG=Search&q=intitle:The+Effect+of+Turbulence+on+Stall+of+Horizontal+Axis+Wind+Turbines#8
32. Pellegrino A, Meskell C. Vortex shedding from a wind turbine blade section at high angles of attack. *J Wind Eng Ind Aerodyn*. 2013;121:131-137. https://doi.org/10.1016/j.jweia.2013.08.002
33. Boorsma K. Comparison of experimental and computational aerodynamic section characteristics of DU91-W2-250 profile. *Master's Thesis*; 2003.
34. Bragg BM, Heinrich DC, Balow FA, Zaman KBMQ. Flow oscillation over an airfoil near stall. *AIAA J*. 1996;34(1):199-201. http://arc.aiaa.org/doi/10.2514/3.13045
35. Yon SA, Katz J. Study of the unsteady flow features on a stalled wing. *AIAA J*. 1998;36(3):305-312. http://arc.aiaa.org/doi/abs/10.2514/2.372
36. Zaman KBMQ, McKinzie DJ, Rumsey CL. A natural low-frequency oscillation of the flow over an airfoil near stalling conditions. *J Fluid Mech*. 1989;202(403):403-442.
37. Mabey DG. Review of the normal force fluctuations on aerofoils with separated flow. *Prog Aerosp Sci*. 1992;29(1):43-80.
38. Zaman KBMQ. Effect of acoustic excitation on stalled flow over a low-Re airfoil. *AIAA J*. 1987;30(6):1492-1499.
39. Farell C, Fedeniuk SK. Effect of end plates on the flow around rough cylinders. *J Wind Eng Ind Aerodyn*. 1988;28(1-3):219-230.
40. Kubo Y, Miyazaki M, Kato K. Effects of end plates and blockage of structural members on drag forces. *J Wind Eng Ind Aerodyn*. 1989;32(3):329-342.

How to cite this article: Khan MA, Schepers GJ, Simao Ferreira C, Sørensen NN. Spectral analysis of New MEXICO standstill measurements to investigate vortex shedding in deep stall. *Wind Energy*. 2020;23:31–44. https://doi.org/10.1002/we.2409